AIP | Journal of Renewable and Sustainable Energy

Numerical investigation and evaluation of optimum hydrodynamic performance of a horizontal axis hydrokinetic turbine

Suchi Subhra Mukherji, Nitin Kolekar, Arindam Banerjee, and Rajiv Mishra

Citation: Journal of Renewable and Sustainable Energy **3**, 063105 (2011); doi: 10.1063/1.3662100
View online: http://dx.doi.org/10.1063/1.3662100
View Table of Contents: http://scitation.aip.org/content/aip/journal/jrse/3/6?ver=pdfcov
Published by the AIP Publishing

Numerical investigation and evaluation of optimum hydrodynamic performance of a horizontal axis hydrokinetic turbine

Suchi Subhra Mukherji,[1] Nitin Kolekar,[1] Arindam Banerjee,[1,a)] and Rajiv Mishra[2]
[1]*Department of Mechanical and Aerospace Engineering, Missouri University of Science and Technology, Rolla, Missouri 65409, USA*
[2]*Department of Materials Science and Engineering, University of North Texas, Denton, Texas 76203, USA*

(Received 16 February 2011; accepted 28 October 2011; published online 21 November 2011)

The hydrodynamic performance of horizontal axis hydrokinetic turbines (HAHkTs) under different turbine geometries and flow conditions is discussed. Hydrokinetic turbines are a class of zero-head hydropower systems which utilize kinetic energy of flowing water to drive a generator. However, such turbines very often suffer from low-efficiency which is primarily due to its operation in a low tip-speed ratio ($\leq$4) regime. This makes the design of a HAHkT a challenging task. A detailed computational fluid dynamics study was performed using the k-ω shear stress transport turbulence model to examine the effect of various parameters like tip-speed ratio, solidity, angle of attack, and number of blades on the performance HAHkTs having power capacities of $\sim$12 kW. For this purpose, a three-dimensional numerical model was developed and validated with experimental data. The numerical studies estimate optimum turbine solidity and blade numbers that produce maximum power coefficient at a given tip speed ratio. Simulations were also performed to observe the axial velocity ratios at the turbine rotor downstream for different tip speed ratios which provide quantitative details of energy loss suffered by each turbine at an ambient flow condition. The velocity distribution provides confirmation of the stall-delay phenomenon due to the effect of rotation of the turbine and a further verification of optimum tip speed ratio corresponding to maximum power coefficient obtained from the solidity analysis. © *2011 American Institute of Physics*. [doi:10.1063/1.3662100]

I. INTRODUCTION

Conventional hydropower has been considered as a sustainable energy resource for several decades and presently supplies almost 100 GW of energy annually, which accounts for almost 10% of U.S. total energy requirement.[1] However, due to site availability constraints and environmental impact of the dams and reservoirs in the available rivers, it is projected that conventional hydropower systems will be unable to meet the 14% rise in total energy demand until the year 2035.[2] The entire mid-west region of USA has more than 6000 miles of river banks, a significant portion of which being fed by low depth rivers and remains untapped for power generation. This presents an urgent need of a low-head hydropower system that can extract power from low depth rivers to meet the increasing energy requirement. Power from moving waterflow provides such form of hydropower systems where turbines submerged in rivers (hydrokinetic turbines) or tides/oceans (marine current turbines (MCTs)) offer an exciting proposition of utilizing kinetic energy of flowing water to drive a generator without diverting the flow path.[3–5]

[a)]Author to whom correspondence should be addressed. Electronic mail: banerjeea@mst.edu. Tel.: 573-341-4494. FAX: 573-341-4607.

As a result, the system provides flexibility of its usage from conventional hydropower systems where the potential energy of the water was being utilized by constructing dams/reservoirs to generate electricity.

The principle of operation behind hydrokinetic turbines is similar to that of wind turbines in principle; however, since the density of water is 850 times greater than air, hydrokinetic turbines allow for increased energy extraction from a given flow stream. In addition, the flow regimes at which hydrokinetic turbines operate are different to conventional wind turbines. The unidirectional nature of river flow eliminates expensive yawing mechanism for hydrokinetic turbines making it cost effective and structurally simpler. Moreover, hydrokinetic technologies do not require large infrastructure such as dams and powerhouses, which results in significantly faster deployment time and reduced manufacturing and operating costs.[6,7] Another advantage of hydrokinetic turbines is their modular nature which leads to a scalable energy output and continuous energy production under zero static head. These attributes reduce the need of energy storage capacity, and as a result of this, hydrokinetic turbines find increased usage in remote locations.[3,5] However, the primary barrier to commercialization of this technology lies in its low efficiency[8] which is primarily due to its operation in a low tip-speed ratio (TSR) ≤ 4 regime. This makes the design of hydrokinetic turbines a challenging task. Since an efficient and cost-effective energy production is directly related to the proper selection of design parameters, an optimum turbine design is required for effective use under variable flow conditions.

Just as in conventional hydraulic turbines, hydrokinetic turbines are primarily classified based upon the orientation of turbine rotor relative to the primary flow direction. Two types of hydrokinetic turbines are possible depending on their principle of operation: horizontal axis turbine where the axis of rotation is parallel to the primary flow direction[9,10] and vertical axis or cross-flow turbine where the rotational axis is perpendicular to the incoming water.[2,11] The current work focuses on horizontal axis hydrokinetic turbines, henceforth referred to as HAHkTs, due to its relatively higher efficiency, lower incidence losses, less vibration, and more uniform lift forces than its vertical axis counterpart.[5,8,12] As in conventional wind turbines, the blades in HAHkTs move perpendicular to the fluid motion receiving power over the entire cycle of rotation. In contrast, vertical axis turbines involve various reciprocating actions requiring hydrofoil surfaces to back-track against the fluid for part of the cycle which is expected to result in lower efficiency. Thus, the swept area of our HAHkTs always faces the fluid unlike the vertical axis turbines where the swept area is perpendicular to the direction of flow. As a result, part of the swept area for vertical axis turbines is simply being blown around at anon-optimal angle that reduces lift resulting in a lower efficiency than their horizontal counterparts.[8] Our design of HAHkTs is meant for operation in a river stream with a mean speed of $\sim$2 m/s which limits the operation to TSR < 4. A review of available literature on HAWTs (horizontal axis wind turbines) and MCTs reveals that the C_p would be restricted to $\sim$0.25 for low TSR.[9,13–18]

Over the last decade, several experimental and numerical investigations have been reported on horizontal and vertical/cross-flow water turbines from the perspective of flow dynamics and the influence of several non-dimensional parameters on the hydrodynamic performance of the turbines.[11] Non-dimensional parameters studied include: Reynolds number (*Re*) (ratio of inertia force to viscous force), TSR (ratio of blade tip speed to fluid speed), and solidity (ratio of blade chord length times the number of blades to turbine circumference). In addition, the number of blades also plays a critical role in determining the performance of the turbines.[2,11] Consul[11] investigated the influence of solidity on the increased performance of a cross flow turbine using two-dimensional numerical simulation. They reported an increase in maximum power coefficient with an increase in blade number, i.e., greater solidity with entire power curve being shifted to a lower TSR. Hwang[2] performed a two-dimensional numerical study as well as an experimental study to understand the effects of number of blades, the chord length variation, the TSR variation, and the shape of the hydrofoil on the overall performance of a cross-flow turbine. They also reported a similar increase in the power coefficient at a lower TSR with increased rotor solidity. In addition, their experimental results showed good agreement with numerical results with an under-prediction of generated power due to the additional drag forces. Batten discussed the effects of blade pitch angle and changes in camber on stall performance

and delay of cavitation in marine current turbines.[9,17] Their analysis, however, is based on high aspect ratio blades where the flow is nearly two-dimensional and can be modeled using blade element momentum (BEM) theory. Myers[10,19] also performed BEM calculations and an experimental study to determine the power output over a range of flow speeds and blade pitch for horizontal axis marine turbines. Although their pre-stall power measurements agreed well with BEM theory, the post-stall measurements were over-predicted due to the failure of the theoretical model to accurately predict stall-delay under rotational motion. Although not investigated for HAHkTs, near wake aerodynamics have been studied for wind turbines to understand the crucial role of wakes on the performance and physical processes of power extraction from the turbine rotation.[13,20,21] However, no extensive study has been reported to date, which discusses the effect of solidity, angle of attack, blade number, and stall delay on the performance of small HAHkTs. The current work is limited to low capacity turbines $\leq$12 kW primarily due to their usage in military/naval applications and for civilian usage in rural hard to reach communities. A detailed numerical investigation for performance evaluation of low capacity HAHkTs is discussed—the turbines are designed to extract power from an average water depth of 5-10 m.

The optimum operating conditions and geometric characteristics of HAHkTs were determined for the variables such as TSR, solidity, number of blades, and *Re* using computational fluid dynamics (CFD) analysis. The purpose of this study was two-fold: (a) it lays a strong foundation for designing and testing HAHkTs system of $\leq$12 kW capacity with optimum geometric and performance characteristics and (b) provides quantitative details regarding the maximum amount of power that can be extracted from a given flow condition using such turbines under a variety of design conditions with and without an optimized blade design—thus embracing the possibility of having both low (non-optimized) and high cost (optimized) systems that would appeal to a wide range of consumers. The paper is organized as follows: in Sec. II, the mathematical and numerical models associated with hydrodynamic performance of HAHkTs are discussed. Section II also provides detailed information regarding the computational geometry used in this work with primary focus on grid and domain specification, boundary conditions, and the solution discretization methodology. Section III discuss the results obtained from three dimensional numerical simulations. The numerical model was first validated with existing experimental results (in air) followed by a further analysis considering individual effect of the variables discussed above. In conclusion, Sec. IV analyses our findings from the numerical model and provides the implication of turbine TSR, solidity, number of blades, and *Re* on the optimum turbine performance under given operating conditions.

II. NUMERICAL METHODOLOGY

A. Governing equations

The numerical modeling of HAHkTs is complicated due to the rotation of the turbine coupled with turbulence and stall effects. A moving reference frame was incorporated to take this into account and transform an unsteady flow in an inertial (stationary) frame to a steady flow in a non-inertial (moving) frame. A constant rotational speed (Ω) is provided on a steadily rotating flow geometry, and equations of fluid motion have been transformed to a rotating frame as shown below,[22]

$$\nabla \cdot \vec{U}_r = 0, \tag{1}$$

$$\rho\left[\frac{\partial}{\partial t}(\vec{U}_r) + \nabla \cdot (\vec{U}_r \vec{U}_r) + (2\vec{\Omega} \times \vec{U}_r + \vec{\Omega} \times \vec{\Omega} \times \vec{r})\right] = -\nabla p + \nabla \cdot \tau_r, \tag{2}$$

where $\vec{U}_r$ is the relative velocity viewed from rotating reference frame, Ω is the rotational speed of the turbine, $\rho(2\vec{\Omega} \times \vec{U}_r)$ is the Coriolis force, $\rho(\vec{\Omega} \times \vec{\Omega} \times r)$ is the centrifugal force, and ∇p is the pressure gradient across the turbine. The viscous stress tensor (τ_r) is defined as

$$\tau_r = \mu_{eff}[(\nabla\vec{U} + \nabla\vec{U}^T) - \frac{2}{3}\nabla\cdot\vec{U}I], \tag{3}$$

where U is the absolute fluid velocity and I is the identity tensor. The molecular viscosity (μ_{eff}) is the sum of the dynamic viscosity (μ) and the turbulent eddy viscosity (μ_t); μ_t being calculated from a representative turbulence model. Amongst different turbulence models that exist in literature, the k-ω shear stress transport (SST) model was chosen for the analysis due to its capability of providing accurate flow-field predictions under adverse pressure gradient and separated flow conditions both of which are prevalent in HAHkTs.[13,23–27] The k-ω SST model is based on the robust and accurate combination, which uses k-ω model in near wall region[28] and k-ε model in far field region.[23,25,29] For flows having adverse pressure gradients, the level of eddy viscosity primarily determines the accuracy of the turbulence model in predicting flow separation. Since the standard k-ω model fails to predict pressure induced separation, the model was reconstructed enforcing Bradshaw's observation in which turbulent shear stress is proportional to the turbulent kinetic energy in the wake region of the boundary layer.[23] Therefore, using the k-ω formulation, the model solves for the transport of turbulent shear stress which controls the level of eddy viscosity in the outer part of boundary layer. However, since the k-ω model has strong sensitivity to the free-stream value outside the boundary layer, a transformed k-ε model is applied on the far wall region due to its insensitive nature to free stream turbulence.[23,24] The governing equations for k-ω SST model is given by

$$\frac{\partial}{\partial t}(\rho k) + \nabla\cdot(\rho k\vec{U}) = \tau_{ij}\nabla\vec{U} - \beta^*\rho\omega k + \nabla\cdot[(\mu + \sigma_k\mu_t)\nabla k], \tag{4}$$

$$\frac{\partial}{\partial t}(\rho\omega) + \nabla\cdot(\rho\omega\vec{U}) = \frac{\gamma}{\nu_t}\tau_{ij}\nabla\vec{U} - \beta\rho\omega^2 + \nabla\cdot[(\mu + \sigma_\omega\mu_t)\nabla\omega] + 2(1 - F_1)\rho\sigma_{\omega 2}\frac{1}{\omega}\nabla k\nabla\omega, \tag{5}$$

where F_1 denotes the blending function which is designed in such a manner that it assumes the value of unity inside the viscous sub-layer where original k-ω model is activated and it gradually switches to zero in the wake region where transformed k-ε model is activated. The model constants are the same as provided in the original work[23] and are not repeated for the purpose of brevity.

B. Computational detail and flow domain generation

The present study assumes steady, incompressible flow where the numerical solution is carried out by solving conservation equations for mass and momentum by deploying an unstructured grid finite volume methodology using commercial CFD software (Fluent 12.1). The geometrical model was created using Solidworks and meshed in Ansys Workbench. Numerical simulations were performed to obtain flow hydrodynamics for three-dimensional rotating boundary conditions. The choice of hydrofoil for HAHkTs is primarily governed by the geometry that produces maximum lift coefficient (C_L) under the operating range of Re. Previous studies[30–32] used SG-6043 airfoil for the design of small wind turbines due to its capability of producing large C_L in the Re range of 10^5–10^6. Since the Re for our case also lies within this range, the SG-6043 airfoil was selected as a hydrofoil for the HAHkT blades. SG-6043 hydrofoil is a part of a family of untwisted, constant pitch blades. A turbine of radius (R) = 1 m was chosen for the three-dimensional rotational analysis. The computational domain consists of two cylinders; the inner cylinder extending 10 rotor diameters and the outer one extending 11 rotor diameters, respectively, in the axial direction (see Fig. 1(a)). The turbine is placed inside the inner cylinder as shown in Fig. 1(b). Multiple reference frames have been adapted with a stationary outer cylinder and rotating inner cylinder and an interior boundary between the two. It is a steady state approximation where the flow in each moving cell zone is solved using the moving reference frame equations (see Sec. II A). At

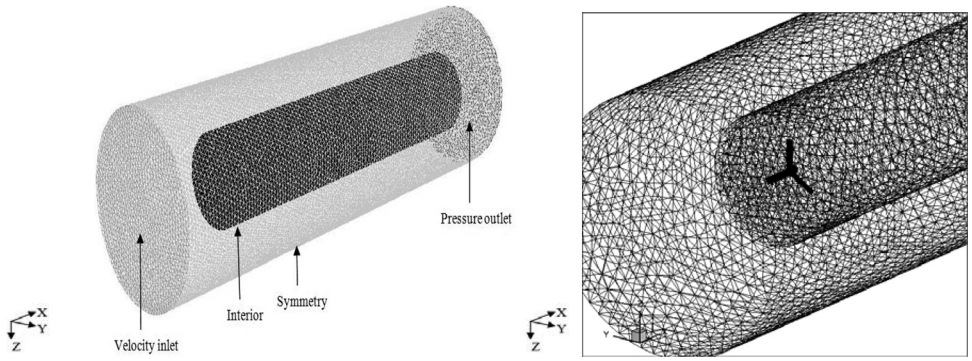

FIG. 1. (a) 3D computational domain along with boundary conditions and (b) grid near the rotor hub.

the interface between the two cell zones, a local reference frame transformation is performed to enable flow variables in the one zone to be used to calculate the fluxes at the boundary of the adjacent zone. Since the boundary between the two zones is conformal, i.e., mesh node locations are identical at the meeting boundary, the interior boundary condition enables particles to pass through the inner boundary to outer one. Velocity inlet and pressure outlet boundary conditions are applied with turbulence specifications same as that for the two-dimensional simulations. A symmetry boundary condition has been provided on the periphery of the outer cylinder indicating zero normal gradients for all flow variables at the symmetry plane. The inner and outer cylinder contains approximately 1.2 and 1.15×10^6 unstructured tetrahedral/hybrid cells. Grid resolution requirements were well established by keeping small enough initial normal spacing from the hydrofoil surface yielding y^+ $(= \rho u_\tau \Delta y/\mu) \sim 120$, where u_τ is the friction velocity and Δy is the cell size. Though this value of y^+ is large, the blending functions included in the k-ω SST model accounted for the unresolved boundary layers on the blades and no separate wall model was used for the computations.

The design of the HAHkTs is based on effective water velocities of 1.75–2.25 m/s as observed in most of the rivers,[4] a mean water speed of $U_\infty = 2$ m/s was chosen for the current work. The left surface was given velocity inlet boundary conditions with turbulence intensity (I) of 3% and length scale (l) of 0.02 m derived from the empirical relationship based on the given flow condition: $I = 0.16(\mathrm{Re})^{-1/8}$ and $l = 0.07L$, where L is computed from the physical dimension of the object, i.e., chord length for the present case. A pressure outlet boundary condition is provided on the right surface with zero gauge pressure and turbulent viscosity ratio is set at a value of 10. A second order upwinding discretization schemes have been employed for all the variables and SIMPLE (Semi-implicit method for pressure linked equation) algorithm was selected for solving pressure-velocity coupling.[33] The PRESTO (pressure staggering options) scheme has been adopted due to its superiority for flows with steep pressure gradient such as the present case.[34] Convergence criteria have been set such that the residuals for the continuity, x-momentum, y-momentum, z-momentum, k, and ω are less than 10^{-4}. Details of the simulation variables are listed in Table I. The rotation of the inner domain adds an additional residual torque to the output torque. In a real-life scenario, the flowing fluid would cause the blade to rotate and the net torque obtained is converted into useful power. For our rotating domain simulations, the turbines blades are, however, subjected to an additional net torque which is a sum of the torque due to the flowing water and the torque due to the rotating domain. The residual torque due to the rotating domain was evaluated for each case by running additional simulations with identical rotational speeds where the free-stream velocity was set to zero. This allowed for evaluating the residual torque due to the rotating domain from these computations. This residual torque was subtracted from the total torque to calculate the net effective torque on the rotor which was used

TABLE I. Parameters for CFD analysis.

Hydrofoil	SG-6043
Density (ρ)	998.2 kg/m^3
Pressure (p)	101.3 kPa
Rotor radius (R)	1 m
Chord length (c)	0.15 m, 0.167 m, 0.2 m, 0.25 m, & 0.3 m
Number of blades (N)	2–4
Blade pitch (θ_P)	10°
Rotor speed (Ω)	3–8 rad/s
Fluid speed (U_∞)	2 m/s
Turbulence model	k-ω SST
Interpolating scheme	2nd order upwind
Pressure scheme	PRESTO
Residual error	1×10^{-4}

for all the power calculations. Table II lists the residual torques for all the cases considered in this study.

C. Governing parameters

The performance of HAHkTs is primarily determined by the power coefficient (C_P) defined as

$$C_P = \frac{P_{out}}{\frac{1}{2}\rho U^3 A}, \tag{6}$$

where P_{out} is power output (kW) of the turbine given by the product of torque generated at the center of the rotor hub and the rotational speed, A is turbine swept area, and U the free-stream velocity. The thrust coefficient (C_T) is defined as

$$C_T = \frac{T}{\frac{1}{2}\rho U^2 A}, \tag{7}$$

where T is the thrust force (N). Turbine TSR is another governing parameter given by

$$TSR = \frac{R\Omega}{U}. \tag{8}$$

In addition, solidity is related to radius (R), blade chord length (c), and number of blades (N) as

TABLE II. Residual torque (N-m) and thrust (N) values due to the rotating domain.

	N = 2		N = 3		N = 4	
TSR	Torque	Thrust	Torque	Thrust	Torque	Thrust
1.5	37.61	248.88	53.05	98.89	58.74	191.84
2.0	65.93	392.59	81.17	185.82	102.83	515.05
2.5	92.85	586.34	119.2	280.25	148.53	344.073
3.0	138.72	751.68	173.19	481.89	233.51	1135.5
3.5	181.43	1146.36	248.92	1165.23	320.21	1525.5
4.0	239.63	1300.54	308.87	1010.43	419.91	1911.03

$$\sigma = \frac{Nc}{2\pi R}. \tag{9}$$

In order to validate the numerical results, the basic performance of our HAHkT model was also evaluated using BEM theory.[12] In BEM theory, the rotor blade was divided into a number of elemental sections, and the torque was calculated from equating the blade forces generated by these blade elements to the momentum changes occurring in the fluid through the rotor disc.[9,12,17] The formulation of BEM theory was based on the assumptions that there is no hydrodynamic interaction between the blade elements; forces on the blades are determined by lift characteristics of the hydrofoil and the drag is zero. The axial induction factor (a) is defined as the fractional decrease in water speed between the free stream and rotor plane,

$$a = 1 - \frac{U_x}{U}, \tag{10}$$

where U_x corresponds to axial velocity behind the rotor plane. The angular induction factor (a') is similarly defined as the fractional increase in angular velocity due to the induced angular velocity at the blades from the conservation of angular momentum. These induction factors a and a' are related to the angle of relative water flow (ϕ) by

$$\tan\phi = \frac{1-a}{(1+a')\lambda_r}; \quad \phi = \theta_P + \alpha, \tag{11}$$

where λ_r is the local tip speed ratio at any radial location r from the rotor hub, θ_P is the turbine pitch ($= 10^\circ$ for present case), and α is the angle of attack. Fig. 2 shows the velocity diagram for the current configuration. For each turbine blade segment, both a and a' are determined in an iterative manner from which C_P is calculated by performing numerical integration of the following expression:

$$C_P = \frac{8}{\lambda^2}\int_{\lambda_h}^{\lambda} \lambda_r^3 a'(1-a)d\lambda_r. \tag{12}$$

The numerical computations were initially carried out with various levels of refinement of mesh in order to obtain a grid independent solution. For the present case, the grid independence study was performed for three dimensional case by calculating the torque generated at the center of the rotor hub using eight different grid sizes with total number of cells (N_{total}) varying between 3.9×10^5 and 4.6×10^6 (see Fig. 3). The fractional change in the magnitude of the torque was calculated based on the formulation

$$\%Error = \frac{|T - T_0|}{T_0} \times 100, \tag{13}$$

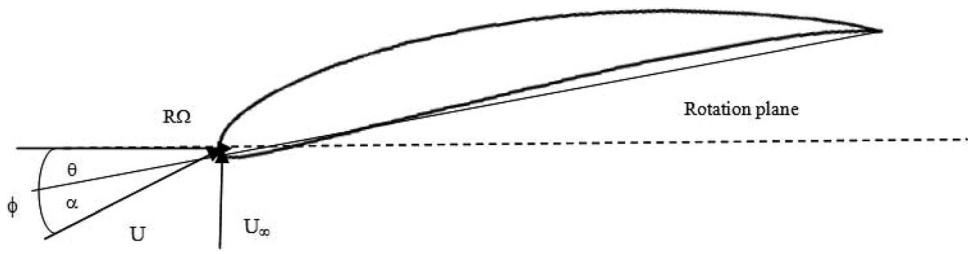

FIG. 2. Velocity diagram for SG-6043 hydrofoil used in current study.

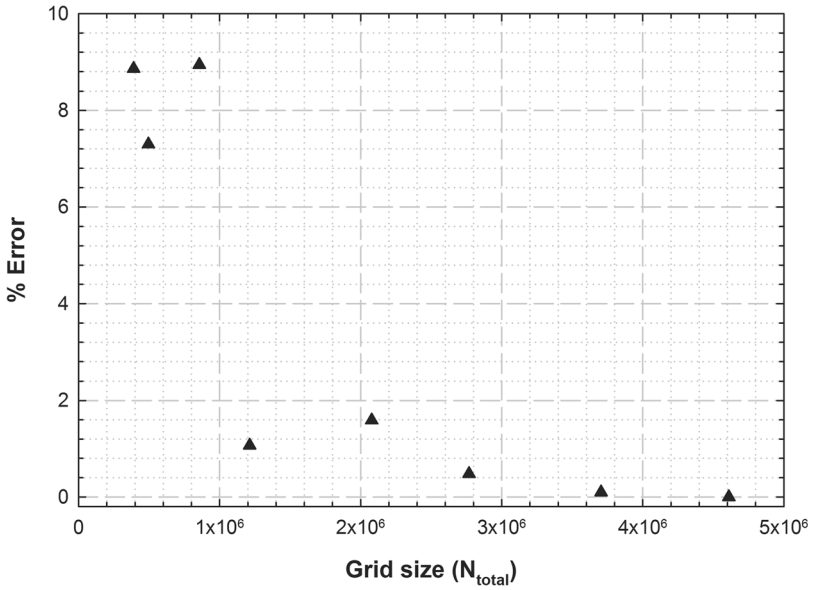

FIG. 3. Grid dependence study for the numerical model using different grid sizes to compute the fractional torque difference (%) from grid independent solution.

where T denotes torque at different grid sizes and T_0 denotes torque correponding to grid independent (maximum grid size) geometry. A grid independent solution with a nearly constant magnitude of torque was observed beyond $N_{total} = 2.7 \times 10^6$ where the difference was $<1\%$, hence suggesting adequate grid resolution for the present study. The computation time for each simulation varied between 6-8 CPU hours when four to six processors were used using Ansys® parallel interface on a machine having 2.4 GHz processor speed and 24 GB of RAM.

III. RESULTS

A. Validation of the three-dimensional numerical model

Before establishing the influence of the non-dimensional variables defined in Sec. II C on turbine performance, the numerical model was validated with experimental results available in the literature. The results were compared with air only experiments of NREL combined phase II data[35]primarily because it used a non-twisted constant non-optimized chord geometry (S809) which resembled our blade design. Furthermore, we also validated our rotating domain model using the NREL combined experimental (phase III) rotor which used an optimized blade. The air only experimental validations were necessitated by the lack of experimental data in the literature on HAHkTs in the low TSR regime (<4). We believe that this provides sufficient validation for our numerical model at this initial design stage; a more rigorous validation using HAHkTs in water is planned in the near future.

The NREL phase II three-bladed horizontal axis wind turbine rotor consists of non-twisted and non-tapered blades using S809 airfoil with constant chord of 0.4572 m.[35] Based on the pressure distribution on the suction and pressure surfaces at various airfoil locations, this particular airfoil produces sufficiently a higher lift coefficient and a lower drag coefficient under a given flow condition. The design of S809 airfoil was primarily made by NREL to perform preliminary hydrodynamic testing of wind turbine subjected to different TSR, solidity, and pitch angle. Since the numerical model discussed in the current work applies to other airfoil profile and fluid medium as well, we performed further experimental validation of our current numerical model incorporating similar geometry and operating conditions as that of NREL phase II rotor. The fixed pitch ($= 12°$) rotor has diameter of 10.1 m which rotates at 72 rpm and rated at 20 kW of electrical power. As observed in Fig. 4, our numerical results agreed quite

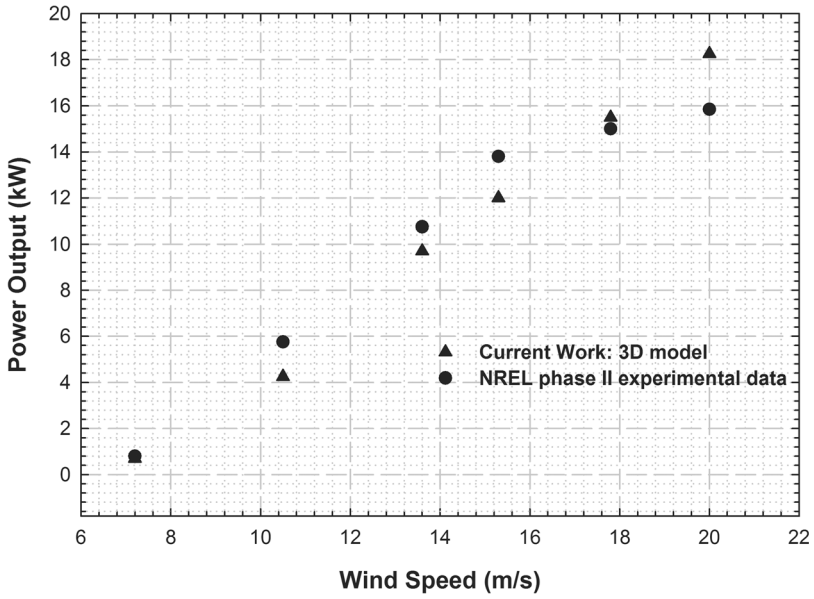

FIG. 4. Comparison of power output (kW) obtained from numerical simulation (with wind) and compared with NREL phase II experimental data.[35]

consistently with experimental data fits over the entire range of wind speeds. A deviation of ~8% was observed between the experimental and numerical results at a wind speed of 22 m/s which might be attributed due to the increased flow incidence resulting in turbine stall phenomena.

The rotating domain model was also used to replicate the experimental results of the NREL combined experimental rotor.[36] This was done primarily to do a one to one comparison where we used an identical blade profile as the experiment, a tapered/twisted blade similar to the NREL report was designed and CFD simulations were run and compared to the reported data. The blade profile included a linear taper and a nonlinear twist distribution, which uses the S809 airfoil from root to tip—an optimized design and was more representative of commercial (wind turbine) blades than our constant chord non-optimized model. The rotor has a diameter of 10.06 m and was composed of 3 blades resulting in a rated power of 20 kW at an operating speed of 72 revolutions/min. Figs. 5 and 6 compares the power output (kW) and the thrust (N) between the experimental data[36] and out CFD simulations over a larger TSR range between 2–8. As can be observed from Fig. 5, the numerical results agreed consistently with the experimental data for the range of TSR values considered. Some discrepancy in the rotor thrust was observed at low TSR values ($\leq$3). We attribute this to limitations in the present numerical model. The multiple reference frame model employed in current analysis is based on the steady state assumption such that the flow at the interface between the adjacent stationary and moving zones is nearly uniform and, hence, does not incorporate any unsteady effects. For the present case, at a lower TSR which is also associated with higher flow incidence (i.e., higher angle of attack), flow separation tends to set in near the stall point. Furthermore, under the rotation of turbine blades, stall-delay phenomena take place on the hydrofoil surface which results in high flow unsteadiness near the turbine rotor region.

1. Comparison with BEM theory

Fig. 7(b) illustrates the validation of thrust coefficient (C_T) for both BEM theory and three-dimensional numerical simulation. Both results show similar increasing trend with C_T increasing with an increase in TSR. In BEM theory, C_T is calculated from equating thrust forces to the product of cross-sectional area and the pressure difference between the two sides of actuator disc. The forces on the turbine blades are determined only by the lift and drag characteristics of

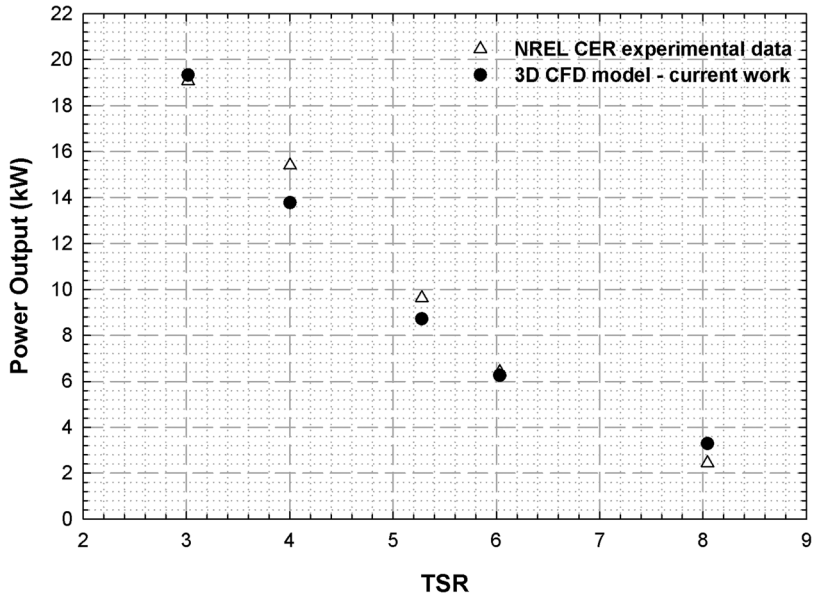

FIG. 5. Comparison of power output (kW) obtained from numerical simulation (with wind) and compared with NREL combined experimental rotor (phase III) data sets.[36]

the hydrofoil. Considering wake rotation, the value of the axial induction factor (a) and the angular induction factor (a') (see Eqs. (10) and (11)) primarily governs the nature of C_T. The numerical model and BEM theory show similar trend. However, a 10%-20% discrepancy is observed between the results. This can be attributed to the fact that BEM theory does not consider the effects on centrifugal and Coriolis forces and over predicts the available power (and hence C_p). The three-dimensional numerical results incorporate both axial and angular induction factors due to rotational motion of the turbine and should be considered to be more accurate than the BEM values.

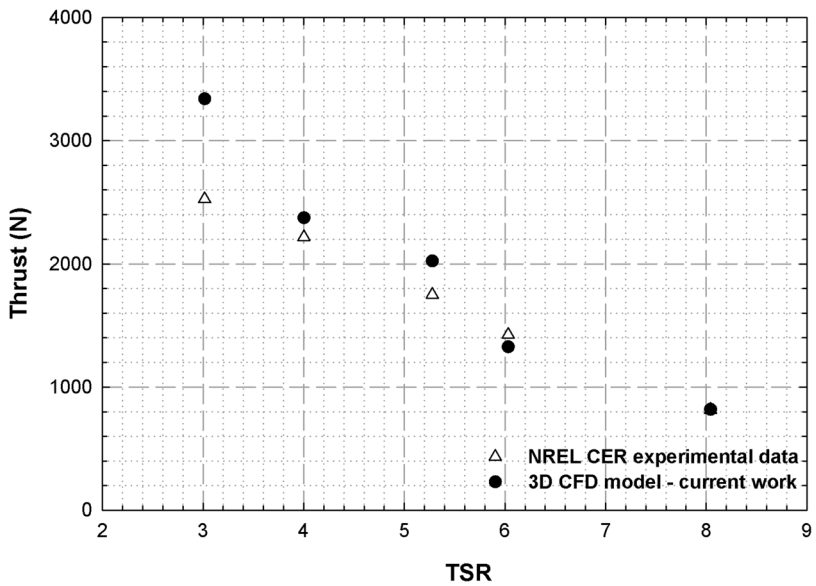

FIG. 6. Comparison of rotor thrust (N) obtained from numerical simulation (with wind) and compared with NREL combined experimental rotor (phase III) data sets.[36]

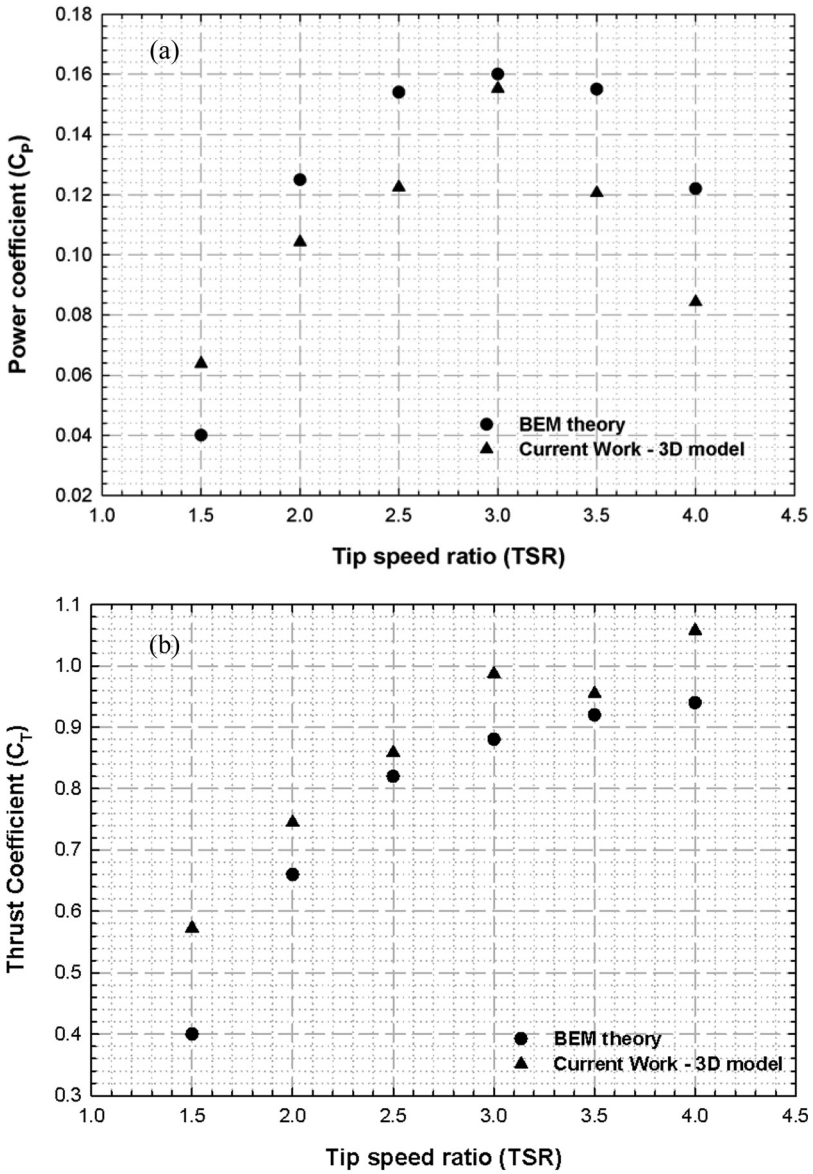

FIG. 7. Comparison of (a) power coefficient and (b) thrust coefficient using both BEM theory and three-dimensional simulations ($N = 3$, $R/c = 5$, and $\boldsymbol{\sigma} = 0.095$).

B. Three-dimensional calculation for performance evaluation

The hydrodynamic performance evaluation of a HAHkT is associated with σ and TSR since these two variables primarily control the volume of fluid which can be utilized for maximum power extraction and, therefore, optimize the turbine efficiency. The power output of a turbine is proportional to the thrust that the turbine exerts on the flow. However, the increase in thrust is also associated with a simultaneous increase in flow impedance resulting in lower energy flux and flow velocity. In order to establish a proper balance between σ and TSR, an intermediate σ at a given flow condition is sought. A turbine of zero σ provides no lift while its infinite solidity counterpart would prevent fluid to flow through rotor plane resulting in zero mechanical work. Thus, in order to examine the influence of σ on turbine performance, three-dimensional numerical simulations were performed using a three-bladed turbine with varying solidity values of 0.12, 0.095, and 0.08, which corresponds to radius to chord ratios (R/c) of 4, 5, and 6, respectively.

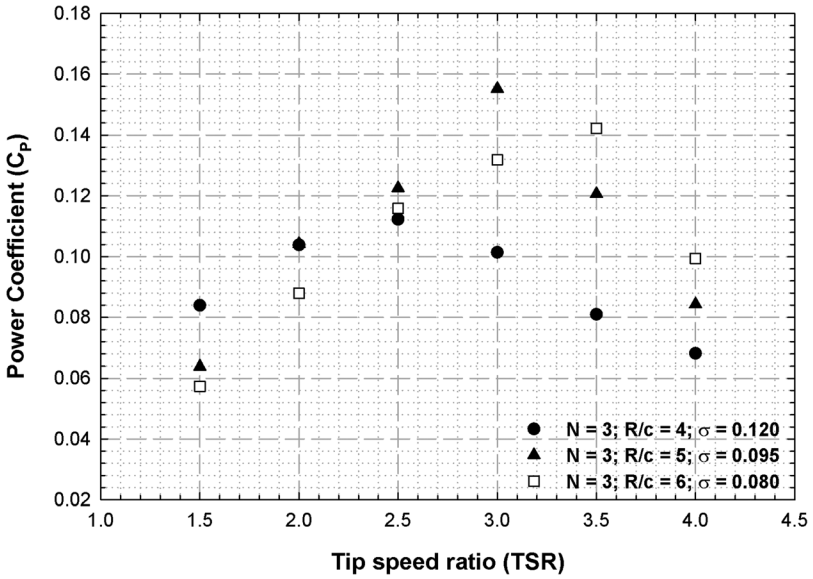

FIG. 8. Variation of power coefficient with tip speed ratio under different turbine solidities.

The results are plotted in Fig. 8. We observe that as σ is increased by $\sim$50% from 0.08 to 0.12 which corresponds to a decrease of R/c from 6 to 4, location of the maximum C_P shifts progressively to lower TSR values. Observing the trend for all three R/c ratios, it can be inferred that a rotor having larger σ generates maximum power at a lower TSR.

A lower TSR results in an increase of angle of attack and, therefore, increased lift and torque for a higher solidity turbine. Increased flow impedance along with a corresponding increase of σ forces the turbine rotor to produce maximum power at a reduced TSR, thereby shifting the maximum C_P towards left. The effect of the number of blades (N) on performance was also investigated using two, three, and four bladed turbines. As shown in Fig. 9, for a constant $\sigma = 0.095$, a three-bladed turbine achieved larger C_P than the ones with two and four blades. Increasing the number of blades beyond $N = 4$ would increase blockage at a constant RPM. As a result, less flow would pass through the turbine decreasing flow entrance velocity at the rotor

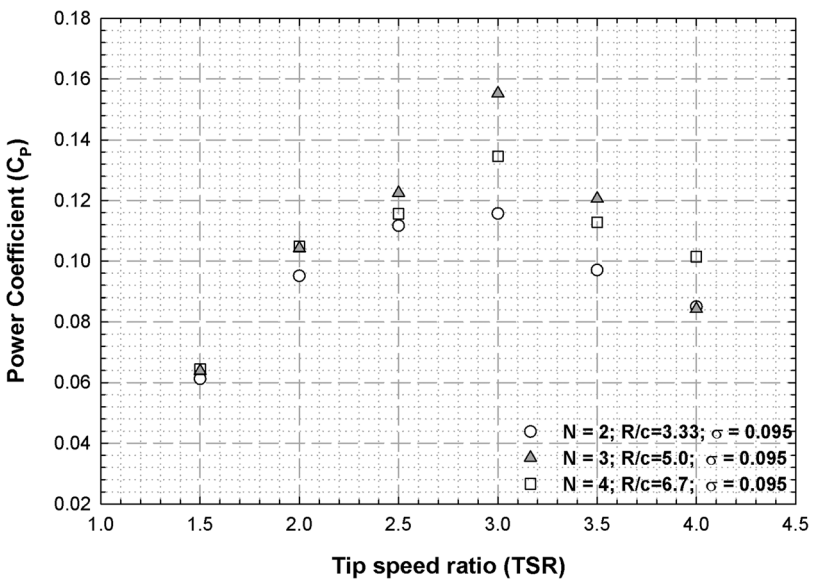

FIG. 9. Effect of number of blades on performance of HAHkTs turbine under constant solidity ($\sigma = 0.095$).

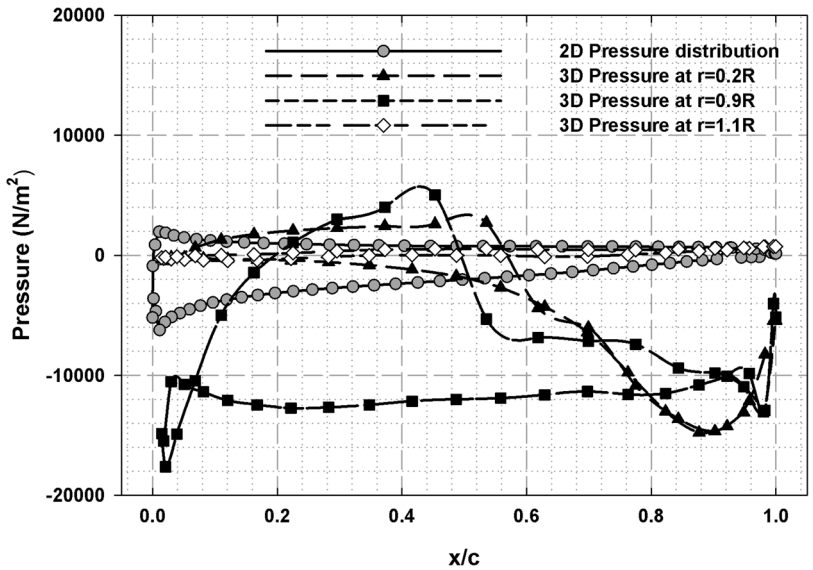

FIG. 10. Pressure distribution along the blade chord obtained from 2D and 3D simulations (TSR = 3, R/c = 5).

plane and ultimately resulting in lesser power extraction. All three turbines, however, produce maximum C_P at a constant TSR = 3.0 since the solidity is held constant. The results also indicate that the initial starting torque of a four bladed turbine is higher than that of the other two cases. This is expected since more blades (solidity) will contribute to larger resistance to motion resulting in increased starting torque at the rotor hub. Since increase in number of blades also corresponds to increase in turbine solidity, the power curve is shifted towards a lower TSR, a feature also observed in Fig. 8. Furthermore, the results obtained from Figs. 8 and 9 provide useful insight for choosing turbine solidity for user-specific applications. Higher solidity turbines will be used when higher initial starting torque and lower rotational speed are required such as water pumping.[37] On the contrary, lower solidity turbines should be considered where lower torque and higher rotational speeds are necessary such as the production of electricity.

Fig. 10 shows the pressure distribution obtained from the two-dimensional and three-dimensional runs performed for a value of $\alpha = 18^\circ$ and identical Re equal to 4×10^5. The x/C of zero corresponds to the leading edge position of the blade. The pressure is plotted along the chord at various radial locations ($r = 0.2$ R, 0.9 R) along the blade span. As can be seen in Fig. 10, the pressure distribution obtained from 3D analysis is higher than the 2D pressure due to

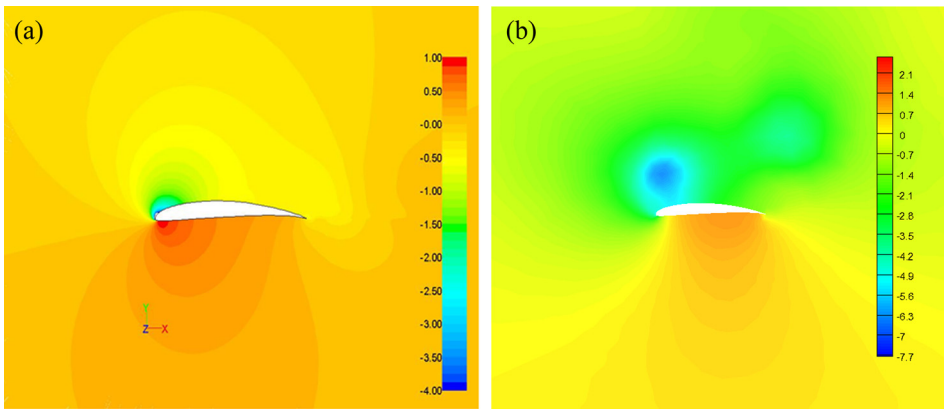

FIG. 11. Comparison of pressure coefficient contours for (a) two-dimensional (stationary), and (b) three-dimensional (rotating) conditions for 18° angle of attack.

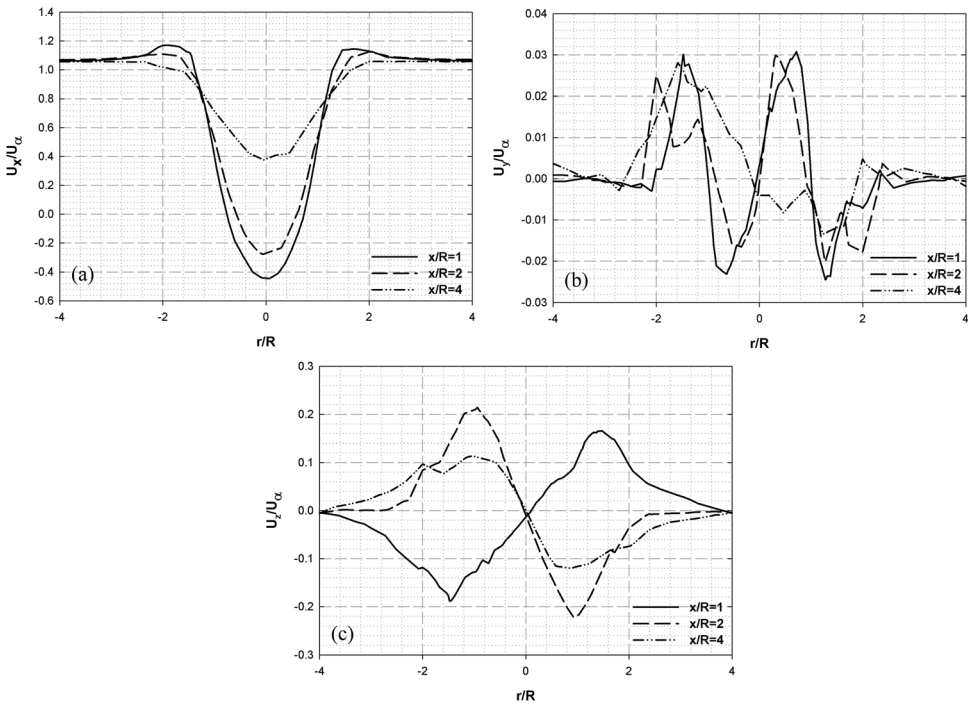

FIG. 12. (a)-(c) Axial, radial, and tangential velocity distributions at different downstream locations calculated at TSR = 3.

consideration of rotational effects. As described earlier in Sec. III A, the stall-delay phenomenon for the three-dimensional rotating condition is effectively a consequence of centrifugal acceleration causing radial flow along the blade span and Coriolis acceleration causing the flow in the chord-wise direction. This delays flow separation to a location further downstream. The two-dimensional stationary condition also fails to predict the exact location of peak axial velocity deficit since the suction side of the hydrofoil is subjected to greater velocity deficit than the pressure side. This results in a rightward shift of peak axial velocity distribution for the stationary condition and indicates that the maximum velocity deficit occurs at a positive radial location near to the pressure side of the hydrofoil. The prediction of stall-delay phenomenon for two-dimensional and three-dimensional cases can be further verified by observing their pressure coefficient contours as shown in Fig. 11. For $\alpha = 18°$, a small pressure drop (negative pressure coefficient) can be observed very near to the leading edge in the two-dimensional case (Fig. 11(a)) indicating the point of flow separation. However, the effect of rapid pressure drop in three-dimensional condition (Fig. 11(b)) is enhanced and dispersed across the entire suction surface due to the effect of turbine rotation causing an even larger pressure drop.

Figs. 12(a)–12(c) illustrates the normalized three dimensional velocity distribution U_x/U_∞, U_y/U_∞, and U_z/U_∞ at the downstream axial locations of $x/R = 1$, 2, and 4, respectively. The axial velocity deficit behind the turbine rotor confirms the expansion and decay of wake phenomenon. The width of the wake increases and axial velocity deficit decreases with increase in downstream distance. In addition, with an increase in radial distance from rotor hub, the axial velocity (Fig. 12(a)) gradually attains the value of an undisturbed flow resulting in a flattening

TABLE III. Axial velocity ratio (U_x/U_∞) for different number of blades at $x/R = 2$.

TSR	2	2.5	3	3.5	4
N = 2	0.77	0.67	0.54	0.49	0.46
N = 3	0.70	0.41	0.38	0.39	0.45
N = 4	0.36	0.35	0.39	0.38	0.59

TABLE IV. Energy loss (in %) to the turbine for different number of blades under the operating range of TSR at $x/R = 2$.

TSR	2	2.5	3	3.5	4
N = 2	41.29	55.27	70.55	76.09	79.09
N = 3	50.79	82.86	85.31	84.92	79.40
N = 4	87.06	87.63	84.78	85.90	64.85

of the velocity profile beyond one rotor diameter in both directions. At $x/R = 4$, a rapid decrease in axial velocity deficit also implies simultaneous disappearance of wake. The magnitude of normal velocity components (see Figs. 12(b) and 12(c)) was observed to be comparatively smaller than the streamwise velocity; a confirmation that the axial velocity distribution has greater influence on the power output, i.e., efficiency of the turbine. At the rotor downstream, the direction of water flow is opposite to that of the rotor, resulting in increased angular momentum in the turbine wake. The flowing water is, therefore, subjected to a normal velocity component along with the axial velocity in stream-wise direction (see Fig. 12(c)). The velocity peaks on both sides of the rotor hub indicate the presence of strong tip vortices on the hydrofoil surface. A localized region with strong tip vortices can be observed where the axial velocity is higher than U_∞ resulting in negative axial induction factor.

The axial velocity deficit for two-bladed, three-bladed, and four bladed turbines under the operating range of TSR is shown in Table III. A larger axial velocity ratio of 0.77 has been observed for TSR = 2 as compared to a ratio of 0.46 as observed for TSR = 4 for a two-bladed turbine. The maximum axial velocity deficit occurs just behind the turbine hub where the maximum amount of energy has been absorbed by the rotor. Increase in number of blades also produces increased flow impedance resulting in an axial velocity ratio of 0.7 for a three-bladed turbine and a value of 0.36 for its four-bladed counterparts (at TSR = 2). This again confirms the effect of blade numbers on turbine performance as shown in Fig. 9. The magnitudes of the axial velocity ratios were utilized to determine the energy loss to the turbine from the mean stream. Assuming the same mass of fluid upstream and downstream of a turbine, a fractional energy loss ($\Delta E/E_0$) can be defined based on the kinetic energy formulation as follows:

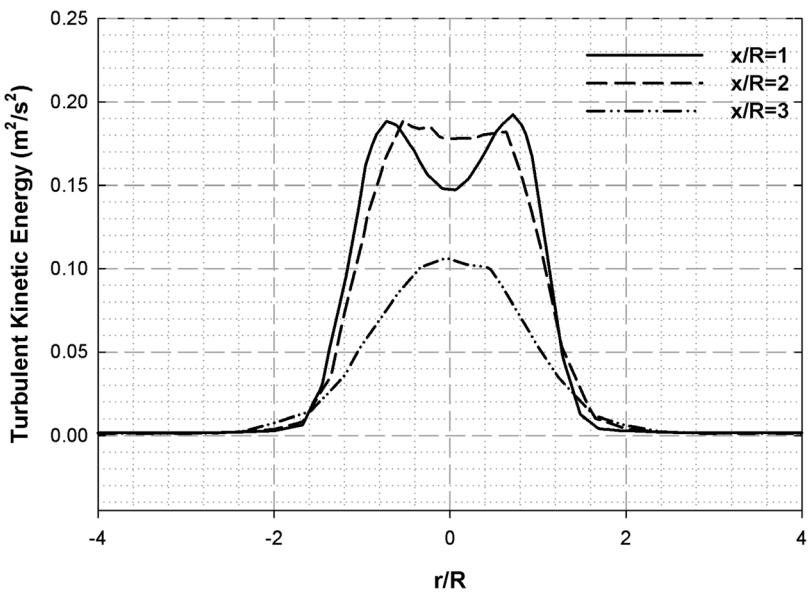

FIG. 13. Turbulent kinetic energy distribution along the radial direction at different rotor downstream locations for TSR = 3.

$$\frac{\Delta E}{E_0} = \frac{U_\infty^2 - U_x^2}{U_\infty^2} \times 100(\%). \tag{14}$$

Based on this formulation, a two-bladed turbine with TSR = 2 incurs ~41.3% energy loss in the wake region behind the turbine at two rotor diameter downstream (see Table IV). However, under the same circumstances, the turbine with TSR = 3 loses 70% of its energy which further confirms higher efficiency of the system. The turbulent kinetic energy can also be obtained along the radial location for different axial positions downstream of the rotor at $x/R = 1$, 2, and 4, respectively. The turbulent kinetic energy profiles in Fig. 13 explain a higher turbulence level in the wake region when compared with non-wake region. A significant increase in turbulent kinetic energy as well as turbulent intensity is observed in the region of wake centerline and also at the tip of the turbine blades due to the formation of the tip vortices.

The turbulence kinetic energy can also be used to identify the transition from the near wake to the far wake. The contours of turbulence kinetic energy and pressure coefficient are plotted in Figs. 14 and 15, respectively, at different axial locations ($x/R = 1$, 2, and 4) within the wake for three different TSR values; the contour plane being parallel to the plane of rotation. The presence of strong vortices can be observed close to the rotor surface, as indicated by large lumps of turbulence kinetic energy and pressure coefficient values near the blade. Under turbine rotation, the rotor decelerates the flow, and the flow begins to rotate in the direction opposite to the rotor. In other words, the wake locations shift in the direction opposite to the direction of rotation of the rotor during the downstream development of the wake. For a turbine operating in a uniform inflow as in our case, the wake consists of root and tip vortices—the contour plots at downstream location $x/R = 4$ shows that the vortices are stable until this

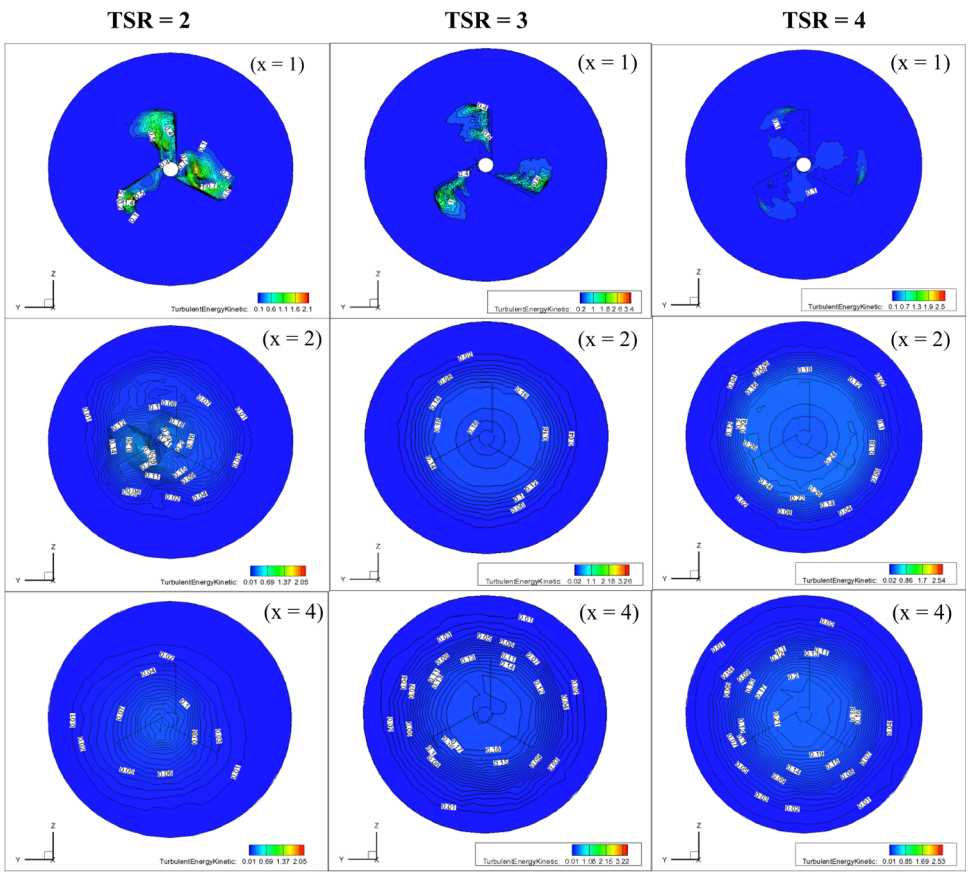

FIG. 14. Contours of turbulence kinetic energy (k) at different axial locations along the rotor downstream ($x/R = 0$, 1, and 4) for TSR = 2, 3, and 4.

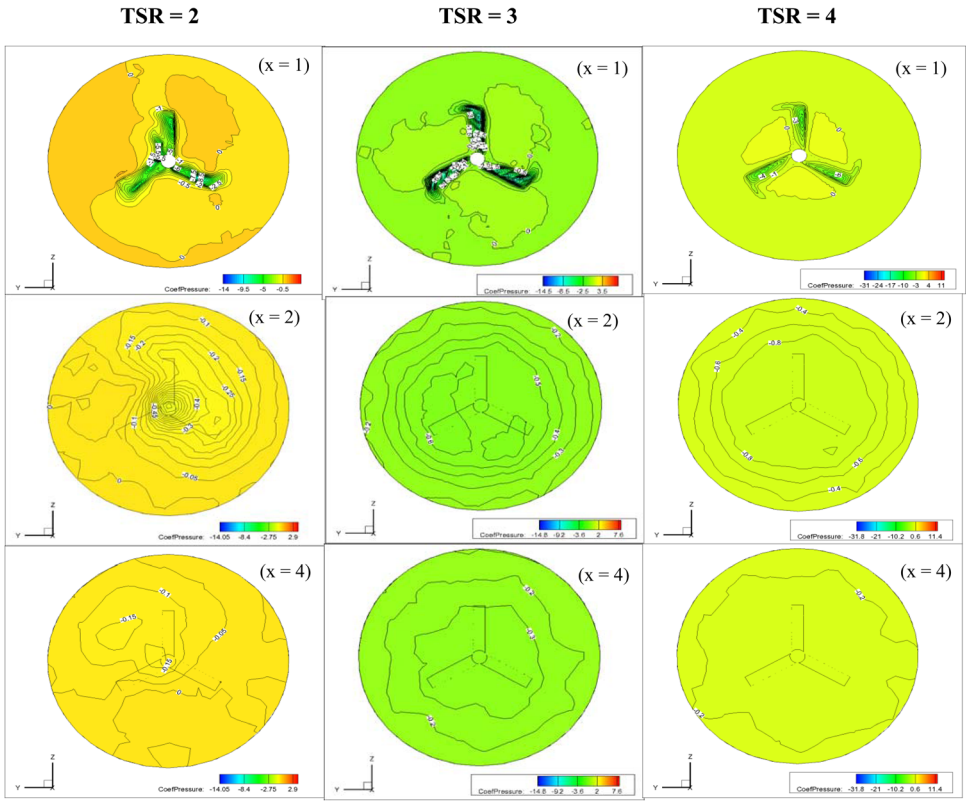

FIG. 15. Contours of coefficient of pressure (C_{pr}) at different axial locations along the rotor downstream ($x/R = 0$, 1, and 4) for TSR = 2, 3, and 4.

location. However, organized structures are not visible, primarily due to the nature of the turbulence model used; the Reynolds averaging procedure smear out any organized structure in the flow. However, a comparison between the contour plots at $x/R = 2$ and $x/R = 4$ reveals that the wake undergoes expansion most likely due to the combination of large scale out of plane motion due to the centrifugal and Coriolis accelerations.

IV. CONCLUSION

Numerical investigations were performed using three-dimensional (rotating) models to examine the performance of HAHkTs under different turbine solidities (0.064–0.127), angle of attack (0°–20°), and blade numbers (2–4). The validation of our numerical model was accomplished by comparing the numerical results using SG-6043 and S-809 airfoil geometries with two distinct wind tunnel data using air as working fluid. The discrepancies observed between the BEM and three-dimensional numerical models result from the turbine rotation which causes stall-delay phenomenon in the latter case under the combined effect of span-wise radial acceleration and chord-wise Coriolis acceleration. However, a reasonably good agreement between the both sets of numerical and experimental studies was observed under the entire operating range of TSR. The three-dimensional results for optimum design have suggested a strong dependence of maximum C_P on TSR when different turbine geometries (i.e., solidity, angle of attack, and number of blades) are being considered. Increase in turbine solidity and blade numbers results in increased C_P under the entire operating range of TSR studied with maximum C_P observed in lower TSR. The study also indicates that lower solidity turbine is preferable for HAHkTs design where low starting torque and high rotating speed are required. Finally, the axial, radial, and tangential velocity distributions along the radial distance at one rotor diameter downstream location has been investigated. The effect of stall-delay phenomenon in three-dimensional model has been confirmed when compared stationary two-dimensional case indicating delay of

separation at further trailing edge of the hydrofoil. In addition, a lesser axial velocity deficit and, hence, a lesser energy loss at higher TSR further confirm higher C_P of HAHkTs.

ACKNOWLEDGMENTS

The authors acknowledge the financial support of Office of Naval Research through Grant No. N000141010923 (Waves, Wind, and Scavengers: Next Generation Renewable Energy Systems for Naval Application; Program manager—Michele Anderson) and the Energy Research and Development Center at Missouri University of Science & Technology (formerly University of Missouri, Rolla) for providing the seed-funding for this project.

[1]J. J. Conti, Annual Energy Outlook 2010: With Projections to 2035, U.S. Energy Information Administration, Office of Integrated Analysis and Forecasting, U.S. Department of Energy, Report No. DOE/EIA-0383 (2010).
[2]I. S. Hwang, Y. H. Lee, and S. J. Kim, Appl. Energy **86**, 1532 (2009).
[3]D. Sale, J. Jonkman, and W. Musial, in Proceedings of the 28th ASME International Conference on Ocean, Offshore and Arctic Engineering, Honolulu, Hawaii (2009), NREL/CP-500-45021, American Society of Mechanical Engineers, New York.
[4]M. J. Khan, M. T. Iqbal, and J. E. Quaicoe, Renewable Sustainable Energy Rev. **12**, 2177 (2008).
[5]M. J. Khan, G. Bhuyan, M. T. Iqbal, and J. E. Quaicoe, Appl. Energy **86**, 1823 (2009).
[6]A. Date and A. Akbarzadeh, Renewable Energy **34**, 409 (2009).
[7]D. G. Hall, K. S. Reeves, J. Brizzee, R. D. Lee, G. R. Carroll, and G. L. Sommers, Wind and Hydropower Technologies: Feasibility assessment of the water energy resources of the United States for new low power and small hydro classes of Hydroelectric plants, Idaho National Laboratory, DOE-ID-11263(2006).
[8]S. L. Dixon, *Fluid Mechanics and Thermodynamics of Turbomachinery*, 5 ed. (Elsevier, Butterworth-Heinemann, MA, 2005).
[9]W. M. J. Batten, A. S. Bahaj, A. Molland, and J. R. Chaplin, Renewable Energy **31**, 249 (2006).
[10]L. Myers and A. S. Bahaj, Renewable Energy **31**, 197 (2006).
[11]C. A. Consul, R. H. G. Willden, E. Ferrer, and M. D. McCulloch, in Proceedings of the 8th European Wave and Tidal Energy Conference, Uppsala, Sweden, 2009.
[12]J. F. Manwell, J. G. McGowan, and A. L. Rogers, *Wind Energy Explained: Theory, Design and Application*. (Wiley, New York, 2002).
[13]L. J. Vermeer, J. N. Sorensen, and A. Crespo, Prog. Aerosp. Sci. **39**, 467 (2003).
[14]J. F. Manwell, J. G. McGowan, and A. L. Rogers, *Wind Energy Explained: Theory, Design and Application*, 2nd ed. (Wiley, New York, 2009).
[15]W. M. J. Batten, A. S. Bahaj, A. F. Molland, and J. R. Chaplin, Ocean Eng. **34**, 1013 (2007).
[16]W. M. J. Batten, A. S. Bahaj, A. F. Molland, and J. R. Chaplin, Renewable Energy **31**, 249 (2006).
[17]W. M. J. Batten, A. S. Bahaj, A. Molland, and J. R. Chaplin, Renewable Energy **33**, 1085 (2008).
[18]A. S. Bahaj, W. M. J. Batten, and G. McCann, Renewable Energy **32**, 2479 (2007).
[19]L. Myers and A. S. Bahaj, Ocean Eng. **34**, 758 (2007).
[20]F. Massouh and I. Dobrev, J. Phys.: Conf. Ser. **75**, 012031 (2007).
[21]D. Hu and Z. Du, J. Hydrodynam. **21**(2), 285 (2009).
[22]C. Thumthae and T. Chitsomboon, Renewable Energy **34**, 1279 (2009).
[23]F. R. Menter, AIAA J. **32**(8), 1598 (1994).
[24]F. R. Menter, AIAA J. **30**(8), 2066 (1992).
[25]Ansys Fluent 12.0 Theory Guide, Ansys Inc. 2009.
[26]E. Ferrer and X. Munduate, J. Phys.: Conf. Ser. **75**, 012001 (2007).
[27]B. Sanderse, Aerodynamics of Wind Turbine Wakes - Literature Review, ECN-E-09-016, Energy Research Center of the Netherlands (2009).
[28]D. C. Wilcox, Turbulence Modeling for CFD (DCW Industries, La Canada, CA, 1993).
[29]B. E. Launder and D. B. Spalding, Comput. Methods Appl. Mech. Eng. **3**, 269 (1974).
[30]P. Giguere and M. S. Selig, J. Sol. Energy Eng. **120**, 108 (1998).
[31]M. M. Duquette, J. Swanson, and K. D. Visser, Wind Eng. **27**(4), 299 (2003).
[32]M. M. Duquette and K. D. Visser, J. Sol. Energy Eng. **125**, 425 (2003).
[33]S. Patankar, Numerical Heat Transfer and Fluid Flow (Hemisphere Publishing Corporation, USA, 1980).
[34]Ansys Fluent 12.0 User's Guide, Ansys Inc. 2009.
[35]E. P. N. Duque, W. Johnson, C. P. vanDam, R. Cortes, and K. Yee, AIAA Paper No. 2000-0038 (2000).
[36]P. Giguère and M. S. Selig, J. Sol. Energy Eng. **120**, 108 (1998).
[37]R. Howell, N. Qin, J. Edwards, and N. Durrani, Renewable Energy **35**, 412 (2010).